

the homologies between NLRC4 oligomerization and prion replication may help to better understand their underlying mechanisms. It remains unknown whether the prion-like mechanism is conserved in other immune NLR sensors for oligomerization. However, one apparent advantage of this mechanism is that a single PAMP or a host-derived danger molecule is sufficient for inducing formation of a fiber assembly, which in principle contains endless ASC because of its self-perpetuation property (39) and thus generates an all-or-none response (40). The requirement of ligand for initiation of this activity could serve to minimize inadvertent activation of an NLR protein through intermolecular collisions.

## REFERENCES AND NOTES

- K. Schroder, J. Tschopp, *Cell* **140**, 821–832 (2010).
- L. Franchi, R. Muñoz-Planillo, G. Núñez, *Nat. Immunol.* **13**, 325–332 (2012).
- V. A. Rathinam, S. K. Vanaja, K. A. Fitzgerald, *Nat. Immunol.* **13**, 333–342 (2012).
- J. von Moltke, J. S. Ayres, E. M. Kofoed, J. Chavarría-Smith, R. E. Vance, *Annu. Rev. Immunol.* **31**, 73–106 (2013).
- B. K. Davis, H. Wen, J. P. Ting, *Annu. Rev. Immunol.* **29**, 707–735 (2011).
- M. Lamkanfi, V. M. Dixit, *Annu. Rev. Cell Dev. Biol.* **28**, 137–161 (2012).
- T. Strowig, J. Henao-Mejia, E. Elinav, R. Flavell, *Nature* **481**, 278–286 (2012).
- H. Wen, J. P. Ting, L. A. O'Neill, *Nat. Immunol.* **13**, 352–357 (2012).
- F. Martinon, K. Burns, J. Tschopp, *Mol. Cell* **10**, 417–426 (2002).
- O. Danot, E. Marquet, D. Vidal-Inglis, E. Richet, *Structure* **17**, 172–182 (2009).
- N. Yan, Y. Shi, *Annu. Rev. Cell Dev. Biol.* **21**, 35–56 (2005).
- W. Chuenchor, T. Jin, G. Ravilious, T. S. Xiao, *Curr. Opin. Immunol.* **26**, 14–20 (2014).
- Z. Hu et al., *Science* **341**, 172–175 (2013).
- X. Cai et al., *Cell* **156**, 1207–1222 (2014).
- A. Lu et al., *Cell* **156**, 1193–1206 (2014).
- L. Franchi et al., *Nat. Immunol.* **7**, 576–582 (2006).
- K. L. Lightfield et al., *Nat. Immunol.* **9**, 1171–1178 (2008).
- E. A. Miao et al., *Nat. Immunol.* **7**, 569–575 (2006).
- E. A. Miao et al., *Proc. Natl. Acad. Sci. U.S.A.* **107**, 3076–3080 (2010).
- A. B. Molofsky et al., *J. Exp. Med.* **203**, 1093–1104 (2006).
- T. Ren, D. S. Zamboni, C. R. Roy, W. F. Dietrich, R. E. Vance, *PLoS Pathog.* **2**, e18 (2006).
- F. S. Sutterwala et al., *J. Exp. Med.* **204**, 3235–3245 (2007).
- J. Yang, Y. Zhao, J. Shi, F. Shao, *Proc. Natl. Acad. Sci. U.S.A.* **110**, 14408–14413 (2013).
- E. M. Kofoed, R. E. Vance, *Nature* **477**, 592–595 (2011).
- Y. Zhao et al., *Nature* **477**, 596–600 (2011).
- J. L. Tenthorey, E. M. Kofoed, M. D. Daugherty, H. S. Malik, R. E. Vance, *Mol. Cell* **54**, 17–29 (2014).
- E. F. Halft et al., *J. Biol. Chem.* **287**, 38460–38472 (2012).
- S. Yuan, M. Topf, T. F. Reubold, S. Eschenburg, C. W. Akey, *Biochemistry* **52**, 2319–2327 (2013).
- S. Yuan et al., *Structure* **19**, 128–140 (2011).
- Y. Pang et al., *Genes Dev.* **29**, 277–287 (2015).
- S. Qi et al., *Cell* **141**, 446–457 (2010).
- T. F. Reubold, S. Wohlgenuth, S. Eschenburg, *Structure* **19**, 1074–1083 (2011).
- R. E. Vance, *Curr. Opin. Immunol.* **32**, 84–89 (2015).
- L. Zhang et al., *Science* **350**, 404–409 (2015).
- P. Chien, J. S. Weissman, A. H. DePace, *Annu. Rev. Biochem.* **73**, 617–656 (2004).
- S. W. Canna et al., *Nat. Genet.* **46**, 1140–1146 (2014).
- N. Romberg et al., *Nat. Genet.* **46**, 1135–1139 (2014).

- A. Kitamura, Y. Sasaki, T. Abe, H. Kano, K. Yasutomo, *J. Exp. Med.* **211**, 2385–2396 (2014).
- X. Cai, Z. J. Chen, *Trends Immunol.* **35**, 622–630 (2014).
- Q. Yin, T. M. Fu, J. Li, H. Wu, *Annu. Rev. Immunol.* **33**, 393–416 (2015).

## ACKNOWLEDGMENTS

We thank Y. Xu and T. Yang at Tsinghua University Branch of China National Center for Protein Sciences Beijing for data collection and computational support, and X. Li for technical instructions of using the K2-Summit camera. We acknowledge the computational facility support on the Explorer 100 cluster system of Tsinghua National Laboratory for Information Science and Technology. The data presented in this paper are tabulated in the main paper and in the supplementary materials. The EM maps have been deposited in the Electron Microscopy Data Bank with accession codes EMD-3139/3140 for the 12- or 11-protomer PrgJ-NAIP2-NLRC4<sup>FL</sup> complex, EMD-3141/3142 for the 11- or 10-protomer PrgJ-NAIP2-NLRC4<sup>CARD</sup> complex, and EMD-3143 for the

FltC-DO<sub>1</sub>-NAIP5-NLRC4<sup>R288AACARD</sup> complex. This research was funded by the Chinese Ministry of Science and Technology (2014CB910101 to J.C., 2011CB910501 to S.-F.S., and 2012CB917303 to H.-W.W.) and the National Natural Science Foundation of China (31230016 to S.-F.S.). Z.H. was supported by a China Postdoctoral Science Foundation-funded project and the Center for Life Sciences (CLS) Postdoctoral Fellowship Foundation. Q.Z. was supported by the CLS Postdoctoral Fellowship Foundation.

## SUPPLEMENTARY MATERIALS

www.sciencemag.org/content/350/6259/399/suppl/DC1  
Materials and Methods  
Figs. S1 to S18  
Table S1  
References (41–56)

11 May 2015; accepted 14 September 2015  
Published online 8 October 2015  
10.1126/science.aac5489

## REPORTS

## INNATE IMMUNITY

# Cryo-EM structure of the activated NAIP2-NLRC4 inflammasome reveals nucleated polymerization

Liman Zhang,<sup>1,2\*</sup> Shuobing Chen,<sup>3,4\*</sup> Jianbin Ruan,<sup>1,2</sup> Jiayi Wu,<sup>3,4</sup> Alexander B. Tong,<sup>1,2</sup> Qian Yin,<sup>1,2</sup> Yang Li,<sup>1,2</sup> Liron David,<sup>1,2</sup> Alvin Lu,<sup>1,2</sup> Wei Li Wang,<sup>4,5</sup> Carolyn Marks,<sup>6</sup> Qi Ouyang,<sup>3</sup> Xinzheng Zhang,<sup>7</sup> Youdong Mao,<sup>3,4,5†</sup> Hao Wu<sup>1,2†</sup>

The NLR family apoptosis inhibitory proteins (NAIPs) bind conserved bacterial ligands, such as the bacterial rod protein PrgJ, and recruit NLR family CARD-containing protein 4 (NLRC4) as the inflammasome adapter to activate innate immunity. We found that the PrgJ-NAIP2-NLRC4 inflammasome is assembled into multisubunit disk-like structures through a unidirectional adenosine triphosphatase polymerization, primed with a single PrgJ-activated NAIP2 per disk. Cryo-electron microscopy (cryo-EM) reconstruction at subnanometer resolution revealed a ~90° hinge rotation accompanying NLRC4 activation. Unlike in the related heptameric Apaf-1 apoptosome, in which each subunit needs to be conformationally activated by its ligand before assembly, a single PrgJ-activated NAIP2 initiates NLRC4 polymerization in a domino-like reaction to promote the disk assembly. These insights reveal the mechanism of signal amplification in NAIP-NLRC4 inflammasomes.

The nucleotide-binding domain (NBD) and leucine-rich repeat (LRR)-containing protein (NLR) family participates in the formation of inflammasomes that activate caspase-1 for cell death induction and cytokine maturation. NLR family apoptosis inhibitory proteins (NAIPs) are so far the only NLR family members with specifically defined ligands (1–4). NAIP2 detects the inner rod protein of the bacterial type III secretion system, including *Salmonella typhimurium* PrgJ, whereas NAIP5 and NAIP6 detect bacterial flagellin such as *Salmonella typhimurium* FltC (2, 4, 5). NLR family caspase recruitment domain (CARD)-containing protein 4 (NLRC4) was initially found to participate in caspase-1 activation and inter-

leukin (IL)-1 $\beta$  secretion in response to cytoplasmic flagellin (6) and was only recently shown to be the common adapter for NAIPs (2, 4). The NAIP-NLRC4 inflammasomes perform effector functions against intracellular bacteria (7, 8), play protective roles in mouse models of colitis-associated colorectal cancer (9, 10), and serve as a potential strategy in tumor immunotherapy (11). Mutations in NLRC4 also induce auto-inflammatory diseases in humans (10, 12–14).

We assembled the FltC-activated NAIP5-NLRC4 complex and the PrgJ-activated NAIP2-NLRC4 complex with the use of CARD-deleted NLRC4 (NLRC4 $\Delta$ ) to avoid potential CARD-mediated aggregation (Fig. 1A). Either full-length NAIP2 or N-terminal baculovirus inhibitor of apoptosis protein repeat

(BIR) domain-deleted NAIP2 (NAIP2 $\Delta$ BIR) was used. During purification, sucrose gradient fractions showed variable molar ratios between NAIP2 and NLRC4 $\Delta$  (Fig. 1B). The fraction with the highest amount of NLRC4 $\Delta$  relative to NAIP2, by

approximately one order of magnitude, contained mostly single, complete disk-like particles (Fig. 1C and fig. S1A). Similarly, overstoichiometry of NLRC4 $\Delta$  to NAIP5 was observed in the reconstituted FliC-NAIP5-NLRC4 $\Delta$  complex (Fig. 1D), also with mostly complete disks under electron microscopy (fig. S1B). In contrast, our earlier PrgJ-NAIP2-NLRC4 $\Delta$  preparations exhibited much lower NLRC4 $\Delta$ /NAIP2 molar ratios (fig. S1C), with mostly incomplete disks (fig. S1D). Labeling of NAIP2 with 5-nm Ni-NTA gold particles in the PrgJ-NAIP2 $\Delta$ BIR-His-NLRC4 $\Delta$  inflammasome revealed singularly labeled complexes (Fig. 1E). These data, together with the previous report that NAIP5 did not oligomerize in the presence of flagellin (15), demonstrated that a single NAIP exists in each complex, whether in a full disk or a partially assembled disk (Fig. 1F).

We collected cryo-electron microscopy (cryo-EM) data on the PrgJ-NAIP2-NLRC4 $\Delta$  complex (Fig. 1G and figs. S2 and S3A). Reference-free two-dimensional (2D) classification revealed mostly 11-bladed, but also 12- and 10-bladed in-

flammasome complexes (fig. S3B), implying conformational flexibility. From the top or bottom view, an inflammasome disk comprises an inner ring and an outer ring (Fig. 1H); 3D classification yielded models with apparent  $C_{10}$ ,  $C_{11}$ , and  $C_{12}$  symmetries (fig. S2). The individual blades did not show observable differences to indicate the single PrgJ-NAIP2 complex in each disk, probably due to similar domain organizations of NAIP2 and NLRC4 (Fig. 1A). Upon imposing the apparent symmetry, the  $C_{11}$ ,  $C_{12}$ , and  $C_{10}$  reconstructions were refined to resolutions of 4.7 Å, 7.5 Å, and 12.5 Å, respectively (Fig. 2, A to F, and fig. S3, C to G). Local resolution estimation of the  $C_{11}$  reconstruction suggests that the inner ring possesses resolutions of 4.0 to 6.0 Å (Fig. 2A and fig. S4), with secondary structural features consistent with a resolution of at least 6.0 Å (Fig. 2, A to D, and fig. S5). Using the crystal structure of NLRC4 $\Delta$  in the inactive conformation (PDB ID 4KXF) (16), we built and refined an atomic model of the active NLRC4 $\Delta$  (table S1). All structures have a domed center and a prominent

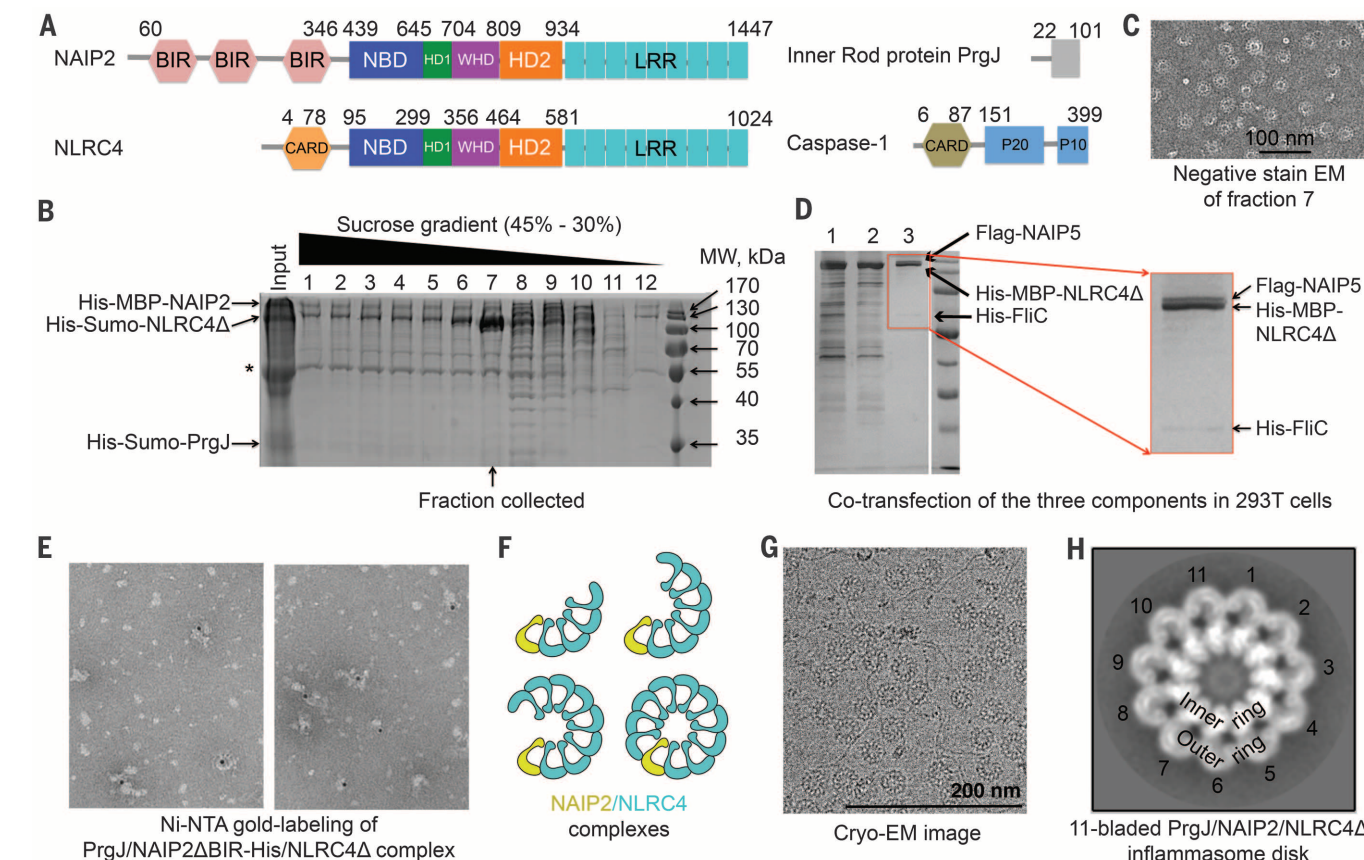


**Fig. 1. Preparation and characterization of NAIP-NLRC4 $\Delta$  complexes.** (A) Domain organizations of *Salmonella typhimurium* PrgJ, mouse NAIP2, mouse NLRC4, and mouse caspase-1. Domain size is drawn approximately to scale; residue numbers are labeled. (B) SDS-polyacrylamide gel electrophoresis (PAGE) of different fractions of the sucrose gradient ultracentrifugation during the purification of the PrgJ-NAIP2-NLRC4 $\Delta$  complex. Locations of the three component proteins are labeled. The asterisk indicates a contaminating band. (C) A representative negative-stain EM image from fraction 7 in (B). (D) SDS-PAGE of amylose resin elution (lane 1), anti-Flag flow-through (lane 2), and anti-Flag

elution (lane 3) fractions during the purification of the coexpressed His-FliC-Flag-NAIP5-His-MBP-NLRC4 $\Delta$  complex. An enlarged image of lane 3 is shown. (E) Ni-NTA gold labeling (5 nm) of purified His-Sumo-PrgJ-NAIP2 $\Delta$ BIR-His-Sumo-NLRC4 $\Delta$  complex upon removal of the His-Sumo tag. (F) Schematic diagram of partial and complete inflammasome particles that contain variable ratios between NAIP2 (yellow) and NLRC4 (cyan). (G) Representative cryo-EM micrograph of PrgJ-NAIP2-NLRC4 $\Delta$  particles. (H) An averaged 2D class of the 11-bladed PrgJ/NAIP2-NLRC4 $\Delta$  inflammasome complex. The dimensions of the image are 43.5 nm  $\times$  43.5 nm.

inner hole (Fig. 2, B, E, and F). The inner ring of the disk contains the NBD, helical domain 1 (HD1), and the winged helix domain (WHD); the outer ring comprises helical domain 2 (HD2) and the LRR domain (Fig. 1A and Fig. 2B).

We focus our further discussions on the 11-bladed structure with the highest resolution. The conformation of active NLRC4 $\Delta$  in the 11-bladed inflammasome exhibits differences from that of inactive NLRC4 $\Delta$  (16). When the NBD-

HD1 regions of NLRC4 in the two states are aligned, the WHD-HD2-LRR module needs to rotate 87.5° along an axis at the junction between HD1 and WHD to turn from the inactive state to the active state (Fig. 2, G and H). The pivot point of the long-range hinge motion is where the inactive and active conformations of the  $\alpha$ 14 helix of WHD intercept (Fig. 2H). The rotation rearranges the intramolecular interactions between WHD and the NBD-HD1 module.

Several missense mutations in human NLRC4 that are associated with auto-inflammatory conditions (12–14)—Thr<sup>337</sup> → Ser, Val<sup>341</sup> → Ala, and His<sup>443</sup> → Pro—localize to this highly dynamic region (fig. S6A).

We do not know whether NLRC4 conformational transition is accompanied by exchange of adenosine diphosphate (ADP) in the inactive state to adenosine triphosphate (ATP) in the active state, as observed for apoptosome assembly by

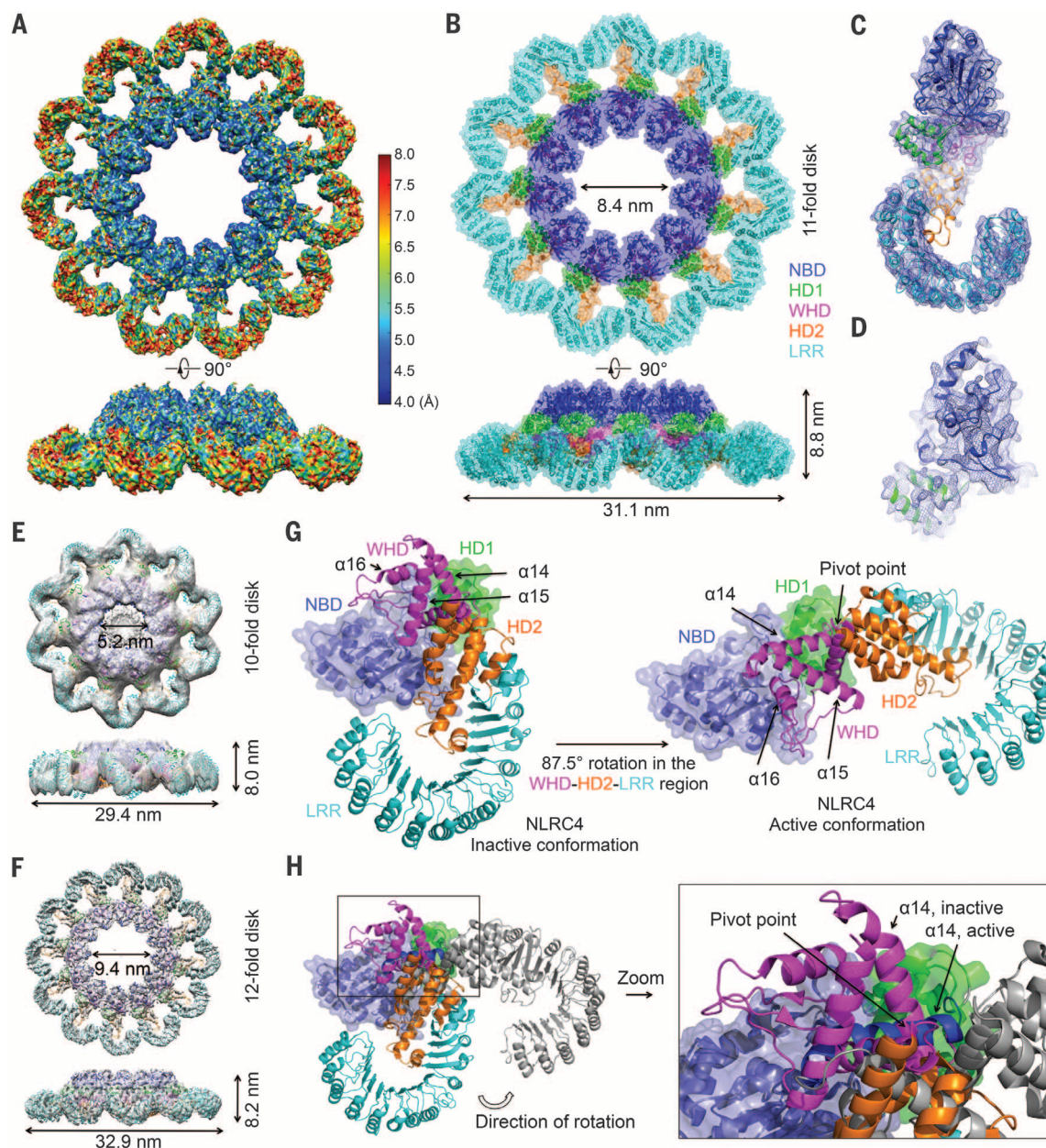


**Fig. 2. Cryo-EM structure determination and conformational activation of NLRC4.** (A) Cryo-EM map of the C<sub>11</sub> PrgJ-NAIP2-NLRC4 $\Delta$  complex colored with local resolution calculated by ResMap using two separately refined half maps. (B) Superimposed ribbon diagram and transparent surface of the C<sub>11</sub> NLRC4 $\Delta$  structure. (C) Cryo-EM density superimposed with one NLRC4 $\Delta$  subunit. (D) A close-up view of the structure of the NBD of NLRC4 $\Delta$  superimposed with the cryo-EM density. (E and F) Cryo-EM maps and fitted NLRC4 $\Delta$  models for the C<sub>10</sub> reconstruction at 12.5 Å resolution (E) and the C<sub>12</sub>

reconstruction at 7.5 Å resolution (F). (G) The WHD-HD2-LRR domain of NLRC4 swings 87.5° to transit from the inactive conformation (left, PDB ID 4KXF) to the active conformation (right). NBD and HD1 are shown in superimposed ribbon diagram and transparent surface, and the WHD-HD2-LRR module is shown in ribbon diagram. (H) Superimposed inactive (colored) and active (gray, except for  $\alpha$ 14 helix, which is in dark blue) conformations of NLRC4 $\Delta$ . The  $\alpha$ 14 helices in the two conformations are labeled to show the relative rotations and the rotational pivot point.

the related adenosine triphosphatase (ATPase) Apaf-1 (17, 18). Lack of nucleotide density in the cryo-EM map, local conformational changes, a modified Walker B motif, and absence of a conserved Arg in the sensor I motif (19) may all suggest alternative mechanisms (fig. S6, B and C). Consistently, the NLRC4 Walker A motif mutant Lys<sup>175</sup> → Arg induced cell killing almost as effectively as did the wild type when coexpressed with NAIP5, flagellin, and caspase-1 (2).

To facilitate analysis on NAIP2-NLRC4 interactions, we generated a homology model of NAIP2ΔBIR based on the NLRC4Δ structure (20) (Fig. 3A). By replacing one of the NLRC4 molecules in the initially fitted C<sub>11</sub> structure, we generated a NAIP2-NLRC4 inflammasome model with one NAIP2 and 10 NLRC4 molecules, in which a single PrgJ-activated NAIP2 initiates NLRC4 activation and polymerization in a domino-like reaction (Fig. 3B). This mechanism differs from other oligomeric ATPases such as apoptosome proteins Apaf-1, CED-4, and DARK, which need to be activated before assembly, either conformationally (by its ligand cytochrome c) or by removal of the inhibitory protein CED-9 (21–23).

The NAIP2-NLRC4 interactions are extensive, with a total surface area of ~1000 Å<sup>2</sup> per subunit per interaction, and contain a mixture of

hydrophobic, hydrophilic, and charged interactions. For brevity, we named one surface as A and the opposing surface as B (Fig. 3C), each comprising a large patch near the NBD and a small patch at the LRR (Fig. 3D). The LRR does appear to play a minor role in strengthening the oligomerization interactions because an LRR-deleted NLRC4 showed attenuation, not abrogation, of killing and oligomerization in comparison with ligand-activated wild-type NLRC4 (2). Calculation of surface electrostatics shows that the NAIP2-A surface, formed by NBD and WHD, is largely basic, whereas the NLRC4-B surface, formed by NBD, HD1, and WHD, is largely acidic; this would suggest that the NAIP2-A surface interacts with the NLRC4-B surface to initiate the directional formation of an inflammasome disk (Fig. 3D). Consistently, the NAIP2-B surface is largely incompatible with either NLRC4-A (fig. S7, A and B) or NAIP2-A (fig. S7, C and D). We thus named NAIP2-A the nucleating surface.

Interaction analysis revealed that residues Lys<sup>613</sup>, Tyr<sup>615</sup>, Arg<sup>631</sup>, Arg<sup>634</sup>, Pro<sup>635</sup>, Tyr<sup>636</sup>, and Gln<sup>778</sup> of NAIP2-A and residues Pro<sup>112</sup>, Asn<sup>116</sup>, Glu<sup>122</sup>, Asp<sup>123</sup>, Asp<sup>125</sup>, Ile<sup>127</sup>, Leu<sup>220</sup>, Leu<sup>313</sup>, Met<sup>349</sup>, and Asp<sup>368</sup> of NLRC4-B bury a large surface area at the interface (Fig. 3E). To test this interface, we used the His-Flu-Flag-NAIP5-His-MBP-NLRC4Δ inflammasome

system because of the availability of differentially tagged constructs for coexpression in 293T cells and because of the sequence similarity between NAIP2 and NAIP5 (Fig. 3F). For NAIP5-A, we mutated Arg<sup>587</sup> and Arg<sup>590</sup>, which correspond to Arg<sup>631</sup> and Arg<sup>634</sup> of NAIP2-A, to Asp (mutation RR2D). For NLRC4-B, we mutated the three acidic residues, Glu<sup>122</sup>, Asp<sup>123</sup>, and Asp<sup>125</sup> to Ala (mutation EDD2A). Whereas the wild-type constructs showed robust copurification of NAIP5 and Fluc by NLRC4, mutations on either NAIP5-A or NLRC4-B reduced the amount of copurified NAIP5 and Fluc (Fig. 3F).

For NAIP2 to initiate NLRC4 polymerization, we hypothesized that it must have weak affinity with the inactive NLRC4. Mapping NLRC4-A and NLRC4-B residues onto the inactive NLRC4 conformation showed that NLRC4-B, but not NLRC4-A, is already largely formed, with only a small part of the WHD in clash with an interacting NAIP2-A (Fig. 3G and fig. S7E). The bound NAIP2-A at this site would push the WHD of NLRC4 exactly at α14, the hinge for conformational changes to occur (Fig. 2, G and H). We propose that the active NAIP2-A surface makes an initial encounter with the NLRC4-B surface in the inactive conformation to initiate the activating conformational change (fig. S7F).

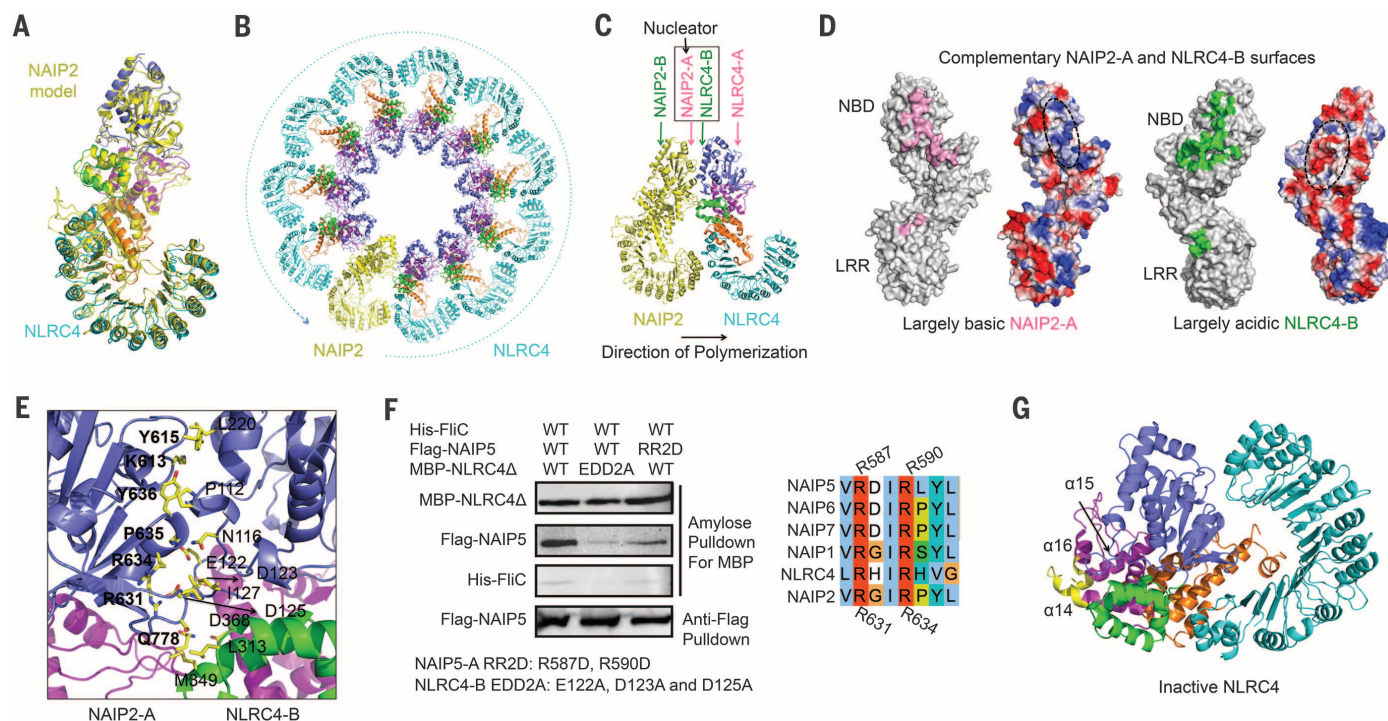


**Fig. 3. Conformational activation of NLRC4 by activated NAIP2.**

(A) Superposition of the NLRC4Δ structure and the NAIP2ΔBIR homology model in the active conformations. (B) A ribbon diagram of the 11-bladed NAIP2-NLRC4 inflammasome disk, with the single NAIP2 molecule in yellow and NLRC4 molecules in cyan. (C) Locations of A and B surfaces, in particular NAIP2-A and NLRC4-B, in the PrgJ-NAIP2-NLRC4Δ inflammasome. (D) Mapped interactions at the NAIP2-A surface (pink) and the NLRC4-B surface (green) and their surface electrostatic potentials. Dotted ovals show the approximate locations of the interface on the electrostatic surfaces. (E) Detailed interactions between the NAIP2-A surface and the

NLRC4-B surface. Those on the A surface are labeled in boldface. (F) Mutations at the NAIP5-A and NLRC4-B surfaces impaired complex formation. The mutated residues in NAIP5 are completely conserved in NAIP2 and NLRC4. The three proteins were coexpressed in 293T cells; the MBP tag was used to pull down the complex, and the component proteins were detected using Western blots. (G) Ribbon diagram of NLRC4Δ in inactive conformation. The region of WHD at the tip of the α14, α15, and α16 helices, in slight clash with an interacting NAIP2, is shown in yellow. Amino acid abbreviations: D, Asp; E, Glu; H, His; I, Ile; K, Lys; L, Leu; M, Met; N, Asn; P, Pro; Q, Gln; R, Arg; S, Ser; V, Val; Y, Tyr.

Calculation of surface electrostatics revealed charge complementarity between the mostly basic NLRC4-A surface and the opposing, largely acidic NLRC4-B surface (Fig. 4, A and B); this finding supports unidirectional polymerization nucleated by NLRC4-A. Structural analysis identified interfacial residues including His<sup>144</sup>, Arg<sup>145</sup>, His<sup>269</sup>, Arg<sup>285</sup>, His<sup>286</sup>, Arg<sup>288</sup>, His<sup>289</sup>, Gln<sup>433</sup>, and Arg<sup>434</sup> of NLRC4-A, and Asn<sup>116</sup>, Glu<sup>122</sup>, Asp<sup>123</sup>, Asp<sup>125</sup>, Ile<sup>127</sup>, Leu<sup>220</sup>, Leu<sup>313</sup>, and Asp<sup>368</sup> of the

opposing NLRC4-B (Fig. 4C). We mutated NLRC4-A residues Arg<sup>288</sup> and His<sup>289</sup> to Asp (mutation RH2D) and Arg<sup>285</sup> to Asp (mutation R285D) and tested their interactions using the same 293T cell coexpression system of His-Flu, Flag-NAIP5, and His-MBP-NLRC4Δ. Both RH2D and R285D mutations reduced the amount of NLRC4Δ in the inflammasome complex (Fig. 4D). Therefore, like a ligand-activated NAIP2, a newly activated NLRC4 triggers activation of another NLRC4 molecule by

inducing conformational changes (fig. S7F). The NBD-NBD interactions between adjacent NLRC4 subunits differ from those in the heptameric apoptosome, with distinct angular relationships that may have explained the existence of more subunits in each NLRC4 disk (21, 22) (fig. S8, A to C).

ASC, like NLRC4, is an inflammasome adapter protein. We showed previously that ASC-dependent inflammasomes activate caspase-1 by ASC<sup>CARD</sup>-mediated caspase-1<sup>CARD</sup> polymerization

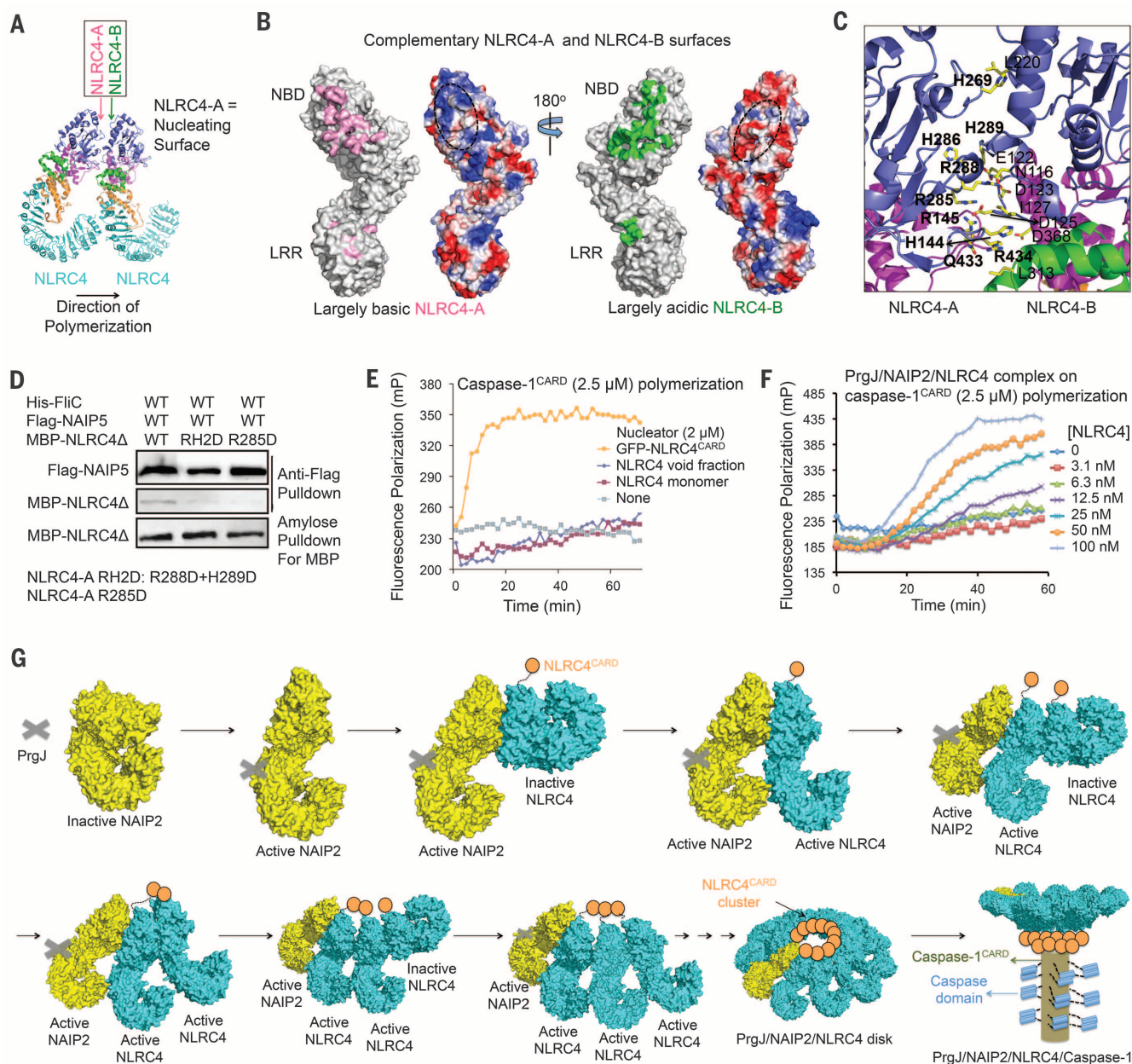


**Fig. 4. NLRC4 polymerization and caspase-1 activation.** (A) Locations of NLRC4-A and NLRC4-B surfaces. (B) Mapped interactions at NLRC4-A (pink) and NLRC4-B (green) surfaces and the surface electrostatic potentials. (C) Detailed interactions between two neighboring NLRC4 molecules. Those on the A surface are labeled in boldface. (D) Mutations at the NLRC4-A surface impaired NLRC4 recruitment. Three proteins were coexpressed in 293T cells. The Flag tag was used to pull down the complex; component proteins were

detected using Western blots. (E) NLRC4<sup>CARD</sup>, instead of NLRC4<sup>FL</sup>, nucleates filament formation of labeled caspase-1<sup>CARD</sup>, as shown by increase in fluorescence polarization. (F) The PrgJ-NAIP2-NLRC4<sup>FL</sup> inflammasome nucleates filament formation of labeled caspase-1<sup>CARD</sup> at substoichiometric ratios, as shown by increase in fluorescence polarization. (G) Schematic diagram for mechanism of PrgJ-NAIP2-nucleated polymerization of NLRC4, followed by caspase-1 dimerization and activation.

(24). To examine whether the PrgJ-NAIP2-NLRC4 inflammasome may directly activate caspase-1 through the CARD in NLRC4, we adopted the same fluorescence polarization assay of caspase-1<sup>CARD</sup> (24). We reconstituted the full-length PrgJ-NAIP2-NLRC4 inflammasome, which showed stacked disk-like structures similar to the previously reconstituted FliC-NAIP5-NLRC4 complex (15) (fig. S8D), and expressed NLRC4<sup>CARD</sup> fused to green fluorescent protein (GFP-NLRC4<sup>CARD</sup>), which was filamentous under EM (fig. S8E). GFP-NLRC4<sup>CARD</sup> augmented the rate of caspase-1<sup>CARD</sup> polymerization, whereas full-length NLRC4 from either the monomeric or the void fraction had little effect (Fig. 4E). The PrgJ-NAIP2-NLRC4 inflammasome robustly promoted filament formation of caspase-1<sup>CARD</sup> even at a 1:100 substoichiometric ratio (Fig. 4F).

Given that NLRC4<sup>CARD</sup> alone is filamentous, we expect that the ~10 molecules of NLRC4<sup>CARD</sup> in each NAIP2-NLRC4 inflammasome form a short filament at the center of the disk. The observed stacking in full-length NAIP-NLRC4 inflammasomes (15) is likely due to interactions between unengaged NLRC4 CARDS. In the presence of caspase-1, the inflammasome may change into single disks, just like the transition of the *Drosophila* apoptosome from double rings to single rings in the presence of the caspase (21). Curiously, the central hole of the inflammasome has a diameter just a bit smaller than that of CARD filaments at ~9 nm, which may provide a perfectly sized “basin” to cradle the protruded CARD filament. These studies demonstrate that ASC-independent NAIP-NLRC4 inflammasomes make use of a similar mechanism for caspase-1 activation, as shown for ASC-dependent inflammasomes (24).

Our studies suggest that activation of NAIP-NLRC4 inflammasomes may proceed through the following steps (Fig. 4G), a conclusion also reached independently by the accompanying study (25): (i) Because of the domain similarity of NAIPs to NLRC4, we propose that the NAIP resting state is similar to the NLRC4 inactive conformation. After a cell is infected and bacterial products appear in the cytosol, a NAIP recognizes its specific bacterial ligand, likely through a surface on the HD1, WHD, and HD2 region (26). The specific ligand drives the NAIP into the open, activated conformation. (ii) The ligand-bound NAIP uses its nucleating surface to interact with the adapter NLRC4 that is yet to be activated. The interaction forces the WHD and its linked C-terminal region to change into the activated conformation, overcoming NLRC4 auto-inhibition. The activated NLRC4 uses its newly exposed nucleating surface to repeat recruitment and activation of additional NLRC4 molecules, until a complete disk is formed or until the NLRC4 concentration falls below the dissociation constant of the interaction. (iii) NLRC4 clustering induces oligomerization of the CARD of NLRC4, enabling the recruitment of caspase-1 through CARD-CARD interactions and triggering caspase-1 dimerization, autoproteolysis, and activation. The activation mechanism ensures signal amplification from the receptor to the adapter, and then to the effector.

As the most abundant energy source in living organisms, ATP is used widely in enzymes to mediate force generation, conformation change, oligomerization, and transport. The ATPase-mediated nucleated polymerization through a domino-like chain reaction identified here adds an important, elegant mechanism to this universal and already complex enzyme family. Nucleated polymerization in NAIP-NLRC4 inflammasomes also presents yet another mode of higher-order oligomerization, which may play a role in facilitating proximity-induced enzyme activation, threshold response, and prion-like propagation in immune signaling (27–30).

## REFERENCES AND NOTES

1. J. D. Gowney, W. F. Dietrich, *Genome Res.* **10**, 1158–1171 (2000).
2. E. M. Kofoed, R. E. Vance, *Nature* **477**, 592–595 (2011).
3. E. Diez et al., *Nat. Genet.* **33**, 55–60 (2003).
4. Y. Zhao et al., *Nature* **477**, 596–600 (2011).
5. J. Yang, Y. Zhao, J. Shi, F. Shao, *Proc. Natl. Acad. Sci. U.S.A.* **110**, 14408–14413 (2013).
6. E. A. Miao et al., *Nat. Immunol.* **7**, 569–575 (2006).
7. E. A. Miao et al., *Nat. Immunol.* **11**, 1136–1142 (2010).
8. L. Franchi et al., *Nat. Immunol.* **13**, 449–456 (2012).
9. B. Hu et al., *Proc. Natl. Acad. Sci. U.S.A.* **107**, 21635–21640 (2010).
10. A. M. Janowski, R. Kolb, W. Zhang, F. S. Sutterwala, *Front. Immunol.* **4**, 370 (2013).
11. J. Garaude, A. Kent, N. van Rooijen, J. M. Blander, *Sci. Transl. Med.* **4**, 120ra16 (2012).
12. S. W. Canna et al., *Nat. Genet.* **46**, 1140–1146 (2014).
13. A. Kitamura, Y. Sasaki, T. Abe, H. Kano, K. Yasutomo, *J. Exp. Med.* **211**, 2385–2396 (2014).
14. N. Romberg et al., *Nat. Genet.* **46**, 1135–1139 (2014).
15. E. F. Halff et al., *J. Biol. Chem.* **287**, 38460–38472 (2012).
16. Z. Hu et al., *Science* **341**, 172–175 (2013).
17. T. F. Reubold, S. Wohlgemuth, S. Eschenburg, *J. Biol. Chem.* **284**, 32717–32724 (2009).
18. Q. Bao, W. Lu, J. D. Rabinowitz, Y. Shi, *Mol. Cell* **25**, 181–192 (2007).
19. M. Proell, S. J. Riedl, J. H. Fritz, A. M. Rojas, R. Schwarzenbacher, *PLOS ONE* **3**, e2119 (2008).

20. M. A. Martí-Renom et al., *Annu. Rev. Biophys. Biomol. Struct.* **29**, 291–325 (2000).
21. S. Yuan, C. W. Akey, *Structure* **21**, 501–515 (2013).
22. S. Yuan et al., *Structure* **19**, 128–140 (2011).
23. S. Qi et al., *Cell* **141**, 446–457 (2010).
24. A. Lu et al., *Cell* **156**, 1193–1206 (2014).
25. Z. Hu et al., *Science* **350**, 399–404 (2015).
26. J. L. Tenthorey, E. M. Kofoed, M. D. Daugherty, H. S. Malik, R. E. Vance, *Mol. Cell* **54**, 17–29 (2014).
27. H. Wu, *Cell* **153**, 287–292 (2013).
28. B. S. Franklin et al., *Nat. Immunol.* **15**, 727–737 (2014).
29. X. Cai et al., *Cell* **156**, 1207–1222 (2014).
30. A. Baroja-Mazo et al., *Nat. Immunol.* **15**, 738–748 (2014).

## ACKNOWLEDGMENTS

We thank G. Bozkurt for technical assistance; H. Ploegh for providing engineered, Ca<sup>2+</sup>-independent sortase and the peptide-fluorophore conjugate Gly-Gly-Gly-TAMRA (GGG-TAMRA); and M. Ericsson for use of the Harvard Medical School EM facility. The data presented in this manuscript are tabulated in the main paper and in the supplementary materials. Cryo-EM maps and atomic coordinates have been deposited in the Electron Microscopy Data Bank (EMDB IDs EMD-6458, EMD-6459, and EMD-6460 for C<sub>11</sub>, C<sub>12</sub>, and C<sub>10</sub> reconstructions, respectively) and Protein Data Bank (PDB ID 3JBL for the C<sub>11</sub> reconstruction). Supported by NIH K99 grant AI08793 (Q.Y.), a Cancer Research Institute postdoctoral fellowship (L.D.), an Intel academic grant, research funds at Peking University, and NIH grant IDP1HD087988. The cryo-EM facility was funded through the NIH grant AI100645 Center for HIV/AIDS Vaccine Immunology and Immunogen Design (CHAVI-ID). The experiments were performed in part at the Center for Nanoscale Systems at Harvard University, a member of the National Nanotechnology Infrastructure Network (NNIN), which is supported by NSF award ECS-0335765.

## SUPPLEMENTARY MATERIALS

www.sciencemag.org/content/350/6259/404/suppl/DC1  
Materials and Methods  
Figs. S1 to S8  
Table S1  
References (31–48)

14 May 2015; accepted 14 September 2015  
Published online 8 October 2015  
10.1126/science.aac5789

## SUPERCONDUCTIVITY

# Metallic ground state in an ion-gated two-dimensional superconductor

Yu Saito,<sup>1</sup> Yuichi Kasahara,<sup>1,2\*</sup> Jianting Ye,<sup>1,3,4†</sup>  
Yoshihiro Iwasa,<sup>1,4‡</sup> Tsutomu Nojima<sup>5‡</sup>

Recently emerging two-dimensional (2D) superconductors in atomically thin layers and at heterogeneous interfaces are attracting growing interest in condensed matter physics. Here, we report that an ion-gated zirconium nitride chloride surface, exhibiting a dome-shaped phase diagram with a maximum critical temperature of 14.8 kelvin, behaves as a superconductor persisting to the 2D limit. The superconducting thickness estimated from the upper critical fields is  $\approx 1.8$  nanometers, which is thinner than one unit-cell. The majority of the vortex phase diagram down to 2 kelvin is occupied by a metallic state with a finite resistance, owing to the quantum creep of vortices caused by extremely weak pinning and disorder. Our findings highlight the potential of electric-field-induced superconductivity, establishing a new platform for accessing quantum phases in clean 2D superconductors.

**R**ecent technological advances of materials fabrication have led to discoveries of a variety of superconductors at heterogeneous interfaces and in ultrathin films; examples include superconductivity at oxide interfaces (1, 2), electric-double-layer interfaces (3), and mechan-

ically cleaved (4), molecular-beam-epitaxy-grown (5, 6), or chemical-vapor-deposited (7) atomically thin layers. These systems are providing opportunities for searching for superconductivity at higher temperatures, as well as investigating the intrinsic nature of two-dimensional (2D)